Air pollution dispersion in Hail city: Climate and urban topography impact

Walid Hassen [a], Nidhal Hnaien [b], Lotfi Ben Said [c,d], Faris Mohammed Albati [e], Badreddine Ayadi [c,f], Wajdi Rajhi [c,g], Lioua Kolsi [c,*]

[a] *Laboratory of Metrology and Energy Systems, Department of Energy Engineering, University of Monastir, Monastir, 5000, Tunisia*
[b] *Department of Energy Engineering, College of Engineering, University of Monastir, Monastir, 5000, Tunisia*
[c] *Department of Mechanical Engineering, College of Engineering, University of Ha'il, Ha'il City, Saudi Arabia*
[d] *Laboratory of Electrochemistry and Environment (LEE), National Engineering School of Sfax, (ENIS), University of Sfax, Sfax, 3038, Tunisia*
[e] *College of Sharia and Law, University of Ha'il, Ha'il City, Saudi Arabia*
[f] *Laboratory of Applied Fluid Mechanics, Environment and Process Engineering "LR11ES57", National School of Engineers of Sfax (ENIS), University of Sfax, Soukra Road Km 3.5, Sfax, 3038, Tunisia*
[g] *Laboratoire de Mécanique, Matériaux et Procédés LR99ES05, Ecole Nationale Supérieure d'Ingénieurs de Tunis, Université de Tunis, 5 Avenue Taha Hussein, Montfleury, 1008, Tunis, Tunisia*

A R T I C L E   I N F O

A B S T R A C T

Due to the rapid urbanization of many cities around the world, industrial manufacturing plants have been expanded quickly, leading to the discharge of large amounts of pollutants into the environment. Consequently, a significant deterioration in local air quality is recorded, representing a high health risk for the city's residents. In this context, the main objective of this work is to understand the dispersion of gas pollution in high-density urban environments, specifically the Hail region of Saudi Arabia. The simulations carried out with Ansys Fluent 19.0 were based on actual climatic conditions, with particular attention paid to accurately reproducing the exact topography of the study area. The main results concern the characterization of flow behavior and the dispersion of gas pollutants emitted by power plants. Several factors, including building geometry and wind speed, are examined. The study reveals that for a reference wind speed of more than 7 m/s, gaseous pollution exhibits a significant tendency to accumulate within buildings, resulting in significant concentrations.

1. Introduction

Air is considered polluted if it undergoes a significant change in composition due to any reason, or if impurities or other gases are mixed with it to the point of harming the life of organisms that live and breathe in it. There are various types of substances that contribute to air pollution. These substances could enter the human body through the respiratory system and directly reach the bloodstream. They can also penetrate the body through the pores of the skin or through the digestive system via contaminated food and drink. Flue gases emitted from factories contain numerous impurities, fumes and suspended solids. These gases frequently contain highly toxic compounds such as arsenic, phosphorus, sulfur, and selenium. They can also transport heavy metal compounds including

---

mercury, lead, as well as suspended particles of cadmium. The quantity of impurities emanating from industrial plants, especially power plants, should not be underestimated. It is estimated that a 1000 MW coal power plant emits approximately 20 tons of sulfur dioxide, 3.5 tons of nitrogen oxides and around 45 tons of fly ash into the air every hour [1]. These values confirm that industrial plants release huge amounts of ash and impurities into the air every day. A significant portion of these pollutants remain suspended in the air and contain numerous substances that are harmful to both the environment and human health. Air pollution dispersion is a significant issue that continues to draw the attention of industrialists and researchers. They are actively seeking effective solutions to reduce impurities, smoke and suspended solids in flue gases emitted from factories and urban sources. Using a CFD modeling, Amorim et al. [2] conducted an analysis of urban trees on the dispersion of air pollution caused by vehicle emission. The authors employed a new numerical model that couples the URban VEgetative canopy module "URVE" with conventional CFD tools to demonstrate that the reduction of carbon monoxide (CO) is strongly influenced by the interaction between meteorological conditions and vegetation density. These results have recently been supported by studies conducted by Taleghani et al. [3], Tiwari et al. [4] and Xing et al. [5].

Sharmilaa et al. [6] reviewed various studies on air pollution caused by emissions produced by road traffic. The characteristics of road traffic in cities, including speed, volume, and vehicle congestion patterns, directly impact CO emissions, which in turn affect the air quality in these urban areas.

The effect of building structure arrangement on air pollution has been analyzed in several papers [7–9]. In fact, it is worth noting that the permeability of buildings and their density are significant factors that affect the accuracy of models used to simulate urban air pollution. Even the geometry of building roofs can have an impact on the air quality in the surrounding areas.

Wen et al. [10] observed that buildings with pitched roofs reduce ventilation, lowering street velocities and turbulence, resulting in higher concentrations of pollution. However, only a few roof configurations can reduce concentrations on the windward side. It has also been demonstrated that the roof slope is significantly correlated with both the average pollution concentrations and their distribution within the street.

The dispersion of air pollution becomes more challenging when cities are located near industrial facilities. The key issue lies in assessing the capability and technological advance of these industrial facilities to reduce the emissions of toxic gases and impurities. Many research groups have devoted time to investigate the efficiency of processes, systems and facilities such as chimneys used for gas emission in industrial plants and power plants. Banerjee et al. [11] proposed two mathematical models, namely the industrial source complex model (ISCST-3) and the Gaussian finite line source model (GFLSM). The simulation results, applied to Pantnagar, India, using these two models indicate that industrial plants contribute approximately 45–70 % of NO_2 emissions.

Issakhov et al. [12] simulated the emission of NO, NO_2, CO, and NO_2, HNO_3, CO_2 during a chemical reaction with oxygen from a thermal power plant. The authors demonstrate that the recorded air pollution caused by these gases increases as the distance to the chimney (emission source) decreases. In the same context, Gourgue et al. [13] demonstrate that the higher the chimney, the lower is the concentration of gases and toxic substances at the urban ground level surrounding the plant. Nevertheless, the concentration of pollution at higher levels can affect the upper floors of tall buildings. Reducing the number of sources with optimized height seems to be a solution to a significant decrease in the concentration of pollution at all levels, including the ground level, as mentioned in Refs. [14–16].

Zair et al. [17] used ANSYS/Fluent calculation code to simulate the emission from a bent chimney impacting on obstacles (buildings). Simulation results have shown that the shape and height of buildings have a significant impact on the dispersion of pollutants in the atmosphere. Therefore, it is preferable for the height of the stack to exceed the height of the buildings in the surrounding area and to have as much distance as possible, in order to facilitate the rapid dispersion of pollutants into the atmosphere. Furthermore, as the distance from the chimney increases, the maximum temperature of the pollutant decreases [18].

Said et al. [19] demonstrated that the flow field around a stack in a crossflow is mainly dominated by the complex interactions between the plume wake, the stack wake, and the downwash effect. This phenomenon occurs when a crossflow passes over the top of the stack.

A new technique for addressing atmospheric pollution while generating free electricity involves the use of solar chimneys. Researchers in Refs. [20–22] have in fact demonstrated that the chimneys of solar power plants have the capability to effectively eliminate atmospheric pollutants on a large scale, particularly fine particulate matter.

According to the conducted literature review, the investigation of pollutant dispersion in real conditions for a very specific climate, such as a desertic and dry environment, has not been sufficiently addressed. Furthermore, the uniqueness of this study lies in simulating an extensive domain, spanning more than 500 ha, with 16 pollution sources. To achieve this objective, a three-dimensional numerical study on Ansys Fluent 19.2 was developed, focusing on the dispersion of gaseous contaminants originating from the power plant chimneys in the city of Hail (Saudi Arabia). The effects of this pollution on the urban areas surrounding the power plants are described in detail. Furthermore, the influence of wind speed on pollutant concentration and air quality is also examined.

2. Methodology

2.1. Studied area

The studied area is located in the Hail region of Saudi Arabia at GPS coordinates 27.46 N, 41.74E. The site measures approximately 3.5 km along the axial direction (x-axis) and 1.5 km along the lateral direction (y-axis), covering a total area of 500 ha. This study zone includes industrial, administrative, and residential buildings (with a height between 3 m and 32 m) surrounding a power plant composed mainly of 16 chimneys (of height 40 m). It should be noted that these chimneys are located less than 600 m from the nearest housing in the northward direction. Fig. 1 shows the schematic view of the studied zone with a scale of 1:22200.
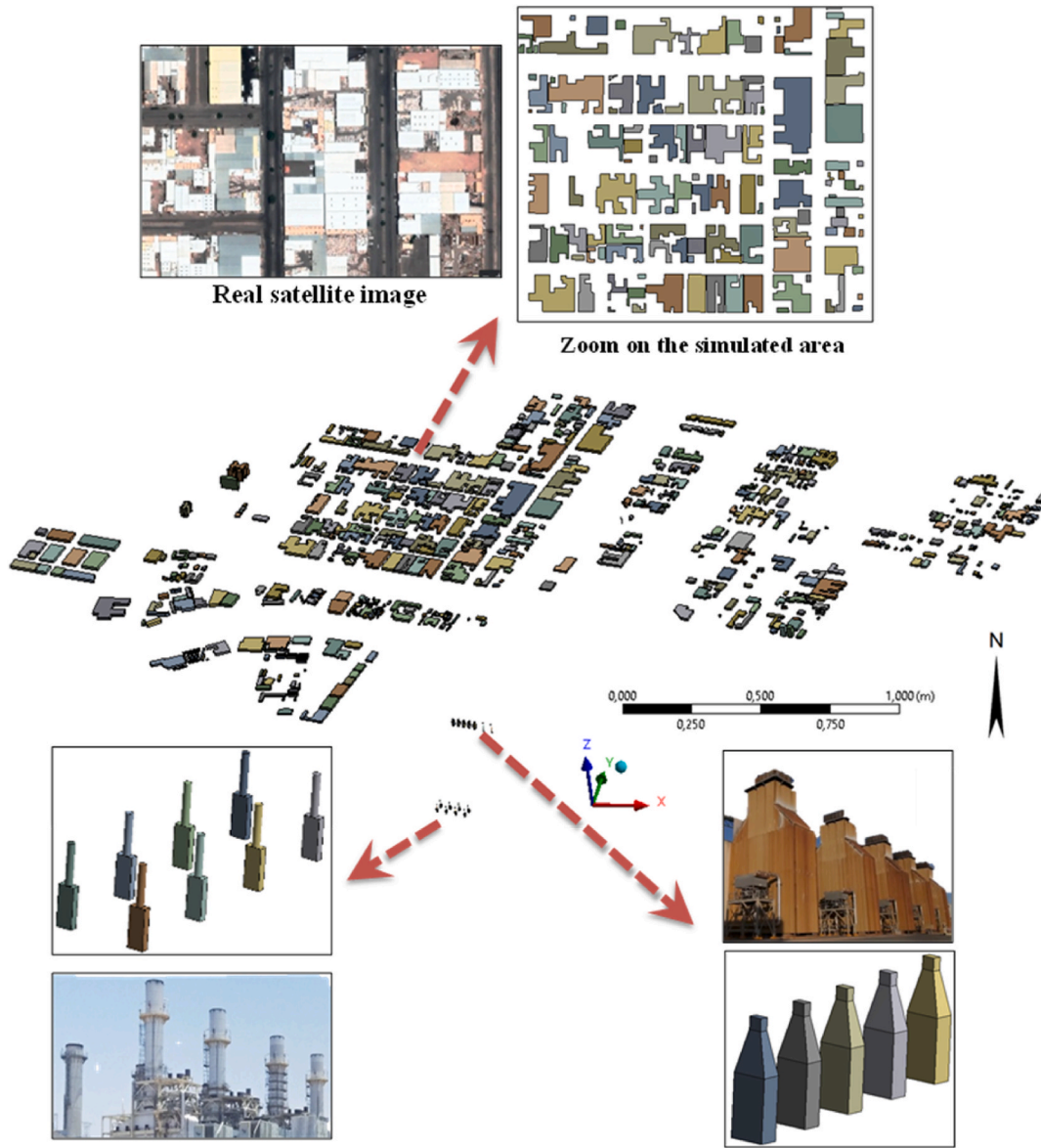
Fig. 1. View and computational domain of the studied area.

2.2. Governing equations

Considering the following assumptions:

- The thermophysical properties of the fluids used (air and gas ejected by the stacks) are considered as constant except for the density which follows the Boussinesq approximation $\rho = \rho_0 + \beta(T - T_0)$.
- Thermal differences due to the temperature gradient between the ground and the ambient air are ignored.
- Flow is turbulent and fully developed.

Using the Cartesian tensor form, the Reynolds-average Navier-Stocks (RANS) equations are expressed as follows:
Continuity equation

$$\frac{\partial}{\partial x_i}(\rho u_i) = 0 \tag{1}$$

Momentum equations

Table 1
Constants values.

α_∞^*	α_∞	α_0	β_∞^*	β_i	R_β	R_k	R_w	ζ^*	M_{t0}	σ_k	σ_w
1	0.52	1/9	0.09	0.072	8	6	2.95	1.5	0.25	2	2

$$\frac{\partial}{\partial x_j}\left(\rho u_i u_j\right) = -\frac{\partial p}{\partial x_i} + \frac{\partial}{\partial x_j}\left[\mu\left(\frac{\partial u_i}{\partial x_j} + \frac{\partial u_j}{\partial x_i} - \frac{2}{3}\delta_{ij}\frac{\partial u_l}{\partial x_l}\right)\right] + \frac{\partial}{\partial x_j}\left(-\overline{\rho u_i' u_j'}\right) + (\rho_0 - \rho)g\delta_{ij} \tag{2}$$

Energy equation

$$\frac{\partial}{\partial x_j}\left(\rho u_j T\right) = \frac{\partial}{\partial x_j}\left[\left(\frac{\mu}{Pr} + \frac{\mu_t}{Pr_t}\right)\frac{\partial T}{\partial x_j}\right] \tag{3}$$

Pr and Pr_t are respectively the Prandtl and the turbulent Prandtl numbers.
Mass fraction equation for each chemical species "s"

$$\frac{\partial}{\partial x_j}\left(\rho u_j f_s\right) = \frac{\partial}{\partial x_j}\left[\left(\frac{\mu}{Sc} + \frac{\mu_t}{Sc_t}\right)\frac{\partial f_s}{\partial x_j}\right] \tag{4}$$

Sc and Sc_t are respectively the Schmidt and the turbulent Schmidt numbers.
The subscript "s" can be: CO_2, CO, H_2O, N_2, NO, NO_2, O_2, or SO_2,
New terms have emerged demonstrating the influence of turbulence. In order to complete the equation system, it is necessary to create a model of the Reynolds stresses.
The Boussinesq approximation is a commonly used method to link the Reynolds stress to the mean velocity gradient.

$$-\overline{\rho u_i' u_j'} = \mu_t\left(\frac{\partial u_i}{\partial x_j} + \frac{\partial u_j}{\partial x_i}\right) - \frac{2}{3}\left(\rho k + \mu_t\frac{\partial u_k}{\partial x_k}\right)\delta_{ij} \tag{5}$$

From the equations provided below, the specific dissipation rate (ω) and turbulent kinetic energy (k) can be determined.

$$\frac{\partial}{\partial x_i}\left(\rho k u_i\right) = \frac{\partial}{\partial x_j}\left(\Gamma_k\frac{\partial k}{\partial x_j}\right) + G_k - Y_k + S_k \tag{6}$$

$$\frac{\partial}{\partial x_i}\left(\rho \omega u_i\right) = \frac{\partial}{\partial x_j}\left(\Gamma_w\frac{\partial \omega}{\partial x_j}\right) + G_\omega - Y_\omega + S_\omega \tag{7}$$

The generation of k and ω caused by the mean velocity gradient is represented by G_k and G_ω in equations (4) and (5). The effective diffusivity and the dissipation for k and ω is denoted by Γ_k, Γ_ω, Y_k and Y_ω respectively. In the current simulation, S_k and S_ω serve as the source terms for the turbulent kinetic energy and the source dissipation ratio, respectively, with the latter assumed to be zero.
To calculate the effective diffusivity in the k-ω model, the following equations are required.

$$\Gamma_k = \mu + \frac{\mu_t}{\sigma_k} \tag{8}$$

$$\mu_t = \alpha^*\frac{\rho k}{\omega} \tag{9}$$

$$\Gamma_\omega = \mu + \frac{\mu_\omega}{\sigma_\omega} \tag{10}$$

here, the turbulent Prandtl numbers for k and ω are denoted by σ_k and σ_ω.

$$\alpha^* = \alpha_\infty^* \left(\frac{\alpha_0^* + Re_t/R_k}{1 + Re_t/R_k}\right) \tag{11}$$

$$Re_t = \frac{\rho k}{\mu \omega} \tag{12}$$

$$\alpha_0^* = \frac{\beta_i}{3} \tag{13}$$

It should be noted that the terms R_k, β_i, α^* and α_∞^* which appear in equations (11)–(13) are constants of the k-ω model. In Table 1, all values of the above-mentioned terms can be found.
It is important to note that the turbulence kinetic energy production (Gk) and its specific dissipation ($G\omega$), in equations (6) and (7), are estimated as follows:

$$G_k = -\rho \overline{u_i' u_j'} \frac{\partial u_j}{\partial x_i} \tag{14}$$

$$G_k = \mu_t S^2 \tag{15}$$

$$S \equiv \sqrt{2 S_{ij} S_{ij}} \tag{16}$$

$$G_w = \alpha \frac{w}{k} G_k \tag{17}$$

$$\alpha = \frac{\alpha_\infty}{\alpha^*} \left(\frac{\alpha_0 + \mathrm{Re}_t / \mathrm{R}_w}{1 + \mathrm{Re}_t / \mathrm{R}_w} \right) \tag{18}$$

where R_ω is constant value given also in Table 1, Re_t and α^* are calculated by equations (11) and (12) respectively. The dissipation of the turbulent kinetic energy Y_k is given by:

$$Y_k = \rho \beta^* f_{\beta^*} k\omega \tag{19}$$

if $\chi_k \leq 0 \, f_{\beta^*} = 1$

if $\chi_k \leq 0 \, f_{\beta^*} = \dfrac{1 + 680 \chi_k^2}{1 + 400 \chi_k^2} \tag{20}$

$$\chi_k \equiv \frac{1}{\omega^3} \frac{\partial k}{\partial x_j} \frac{\partial \omega}{\partial x_j} \tag{21}$$

$$\beta^* = \beta_i^* [1 + \zeta^* F(M_t)] \tag{22}$$

$$\beta_i^* = \beta_\infty^* \left(\frac{4/15 + \left(\mathrm{Re}_t / R_\beta \right)^4}{1 + \left(\mathrm{Re}_t / R_\beta \right)^4} \right) \tag{23}$$

with ζ^*, R_β and β_∞^* are constant values (Table 1). The dissipation of ω is given as follows:

$$Y_w = \rho \beta f_\beta \omega^2 \tag{24}$$

$$f_\beta = \frac{1 + 70 \chi_w}{1 + 80 \chi_w} \tag{25}$$

$$\chi_w = \left| \frac{\Omega_{ij} \Omega_{jk} \Omega_{ki}}{\left(\beta_\infty^* \omega \right)^3} \right| \tag{26}$$

$$\Omega_{ij} = \frac{1}{2} \left(\frac{\partial u_i}{\partial x_j} - \frac{\partial u_j}{\partial x_i} \right) \tag{27}$$

$$\beta = \beta_i \left[1 - \frac{\beta_i^*}{\beta_i} \zeta^* F(M_t) \right] \tag{28}$$

$F(M_t) = 1$ if $M_t \leq M_{t0}$

$F(M_t) = M_t^2 - M_{t0}^2$ if $M_t \succ M_{t0} \tag{29}$

$$M_t^2 = \frac{2k}{a^2} \tag{30}$$

$$a = \sqrt{\gamma R T} \tag{31}$$

Table 1 summarizes the different constants cited above:

Table 2
Boundary conditions.

Boundaries	Velocity	Temperature	Mass fraction	Kinetic energy	Dissipation rate
Chimney	$u = u_0$ $v = 0$ $w = 0$	$T = T_0$	$f = f_0$	$k_0 = \dfrac{3}{2}(Iu_0)^2$	$\omega_0 = \dfrac{k_0^{1/2}}{C_\mu^{1/4} 0.07d}$
Crossflow	$u = u_\infty = u_{ref}(z/z_{ref})^\alpha$ $v = 0$ $w = 0$	$T = T_\infty$	$f = 0$	$k_\infty = \dfrac{3}{2}(Iu_\infty)^2$	$\omega_\infty = \dfrac{k_\infty^{1/2}}{C_\mu^{1/4} 0.07 H_T}$
Obstacles and building	$u = 0$ $v = 0$ $w = 0$	$\dfrac{\partial T}{\partial n} = 0$	$\dfrac{\partial f}{\partial n} = 0$	$k = 0$	$\dfrac{\partial \omega}{\partial n} = 0$
Other boundaries of the domain	$\dfrac{\partial u}{\partial n} = 0$ $\dfrac{\partial v}{\partial n} = 0$ $\dfrac{\partial w}{\partial n} = 0$	$\dfrac{\partial T}{\partial n} = 0$	$\dfrac{\partial f}{\partial n} = 0$	$\dfrac{\partial k}{\partial n} = 0$	$\dfrac{\partial \omega}{\partial n} = 0$

(a)   (b)
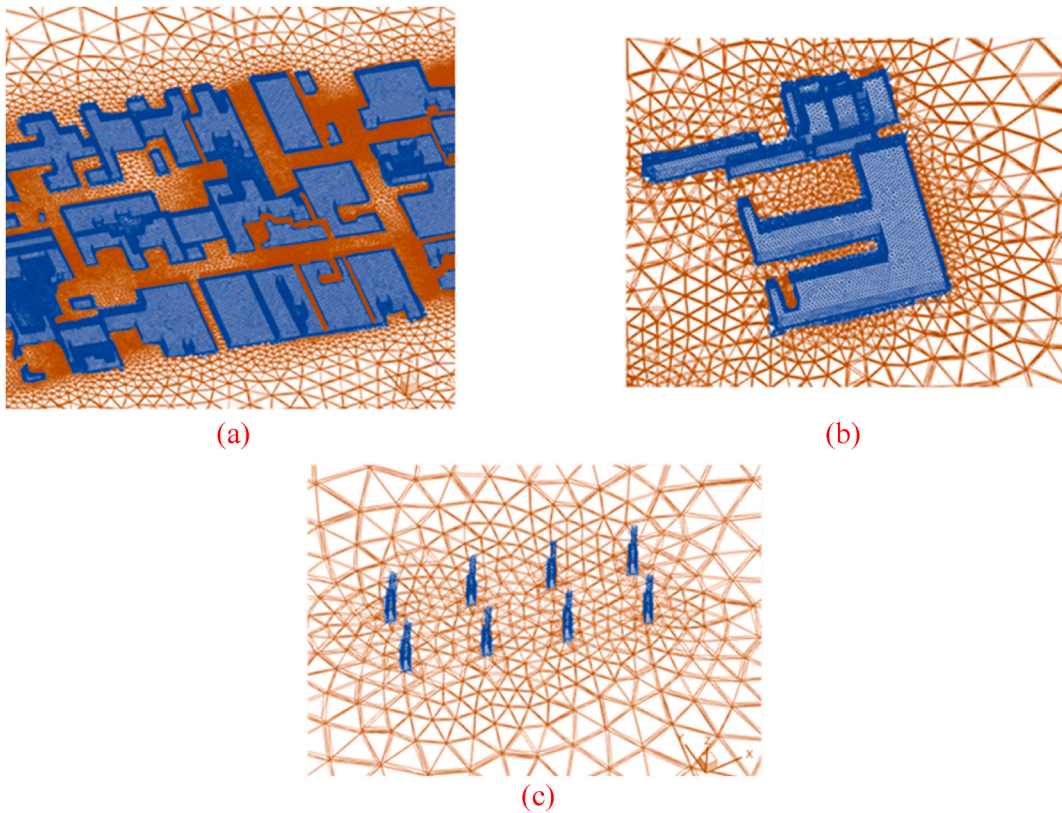

(c)

Fig. 2. Some schematic presentation of the mesh (a) overview of buildings, (b) enlarged view of buildings, (c) chimney's view.

2.3. Boundary conditions

The boundary conditions associated with equations (1)–(31) can be found in Table 2.

In Table 2, the exhaust speed of the gases at the exit of the chimney is considered to be $u_0 = 35$ m/s. The Crossflow velocity simulating the wind, follows a power law model, with the α coefficient equal to 0.25 [23]. Using the Global Wind Atlas in the GPS coordinates of the studied site, we could determine that for an altitude $z_{ref} = 10$ m the speed $u_{ref} \in [0, 7 m/s]$ with an annual average of 3.5 m/s.

For the turbulent kinetic energy, "I" represents the turbulence intensity estimated at 5 % for the climatic condition of Hail region [24]. Finally, the terms d and Ht in the specific dissipation rate equations, represent respectively the hydraulic diameter of the stacks and the altitude of the whole studied area.
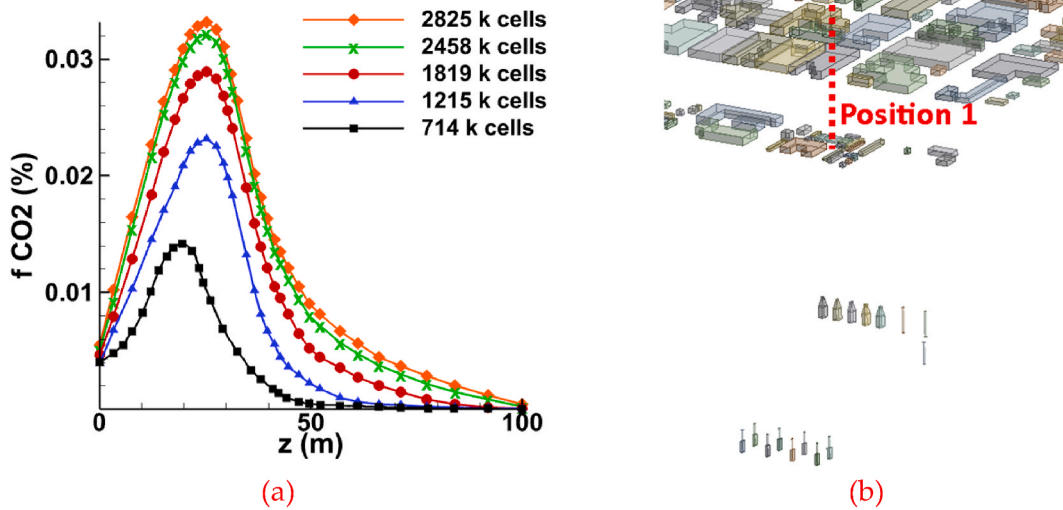
Fig. 3. (a) CO_2 mass fraction profile as a function of altitude in position 1 for different mesh sizes for $u_{ref} = 7$ m/s and $u_0 = 35$ m/s; (b) selected position.
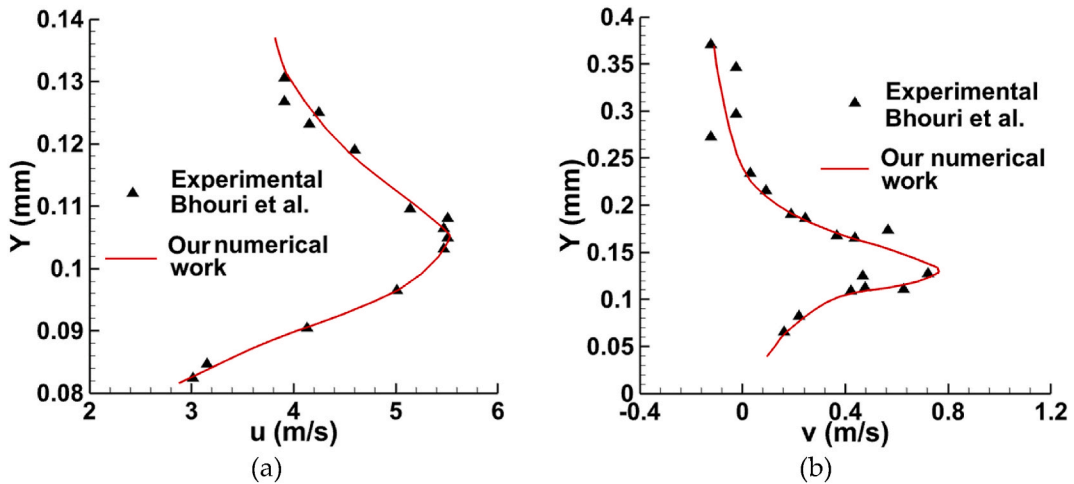

Fig. 4. Average velocity profiles (a) u, (b) v for $U_\infty = 5$ m/s, $U_0 = 8$ m/s on a vertical line located at 60 mm distance from the track.

2.4. Grid distribution

Since the computational domain is very large, we opted for an unstructured mesh to strike a balance between computation time and result accuracy. In the area surrounding the buildings and mainly around the stacks, a refined tetrahedral mesh has been adopted, whereas a less dense mesh has been implemented in other locations (Fig. 2 (a,b,c)). In order to guarantee a high-quality mesh, several restrictions were satisfied, including a skewness below 0.4, a volume ratio under 30, and an aspect ratio under 20.

In order to improve computational efficiency, a sensitivity analysis was conducted to optimize the mesh size. Several tests are represented on Fig. 3, which displays the CO_2 mass fraction as a function of altitude. Position 1, which is located in the middle of the buildings closest to the stacks, was used as the location for the plotting. After computing with several larger grids (714 k, 1215 k, 1819k, and 2458 k), the particular grid of 2825 k cells was ultimately selected. Indeed, the sensitivity analysis conducted on the meshes revealed that the difference between the fine grid of 2458 k and the 2825 k grid is below 5 %.

2.5. Validation tests

For the sake of validation, the numerical results have been compared with the experimental ones of Bhouri et al. [25,26]. In these works, the authors consider a chimney (100 mm tall, 10 mm in diameter) with a parallelepiped obstacle (150 mm tall, 50 mm wide, and 50 mm deep). The obstacle is positioned 10 cm upstream of the chimney. The entire setup is placed inside a 3 m long wind tunnel,
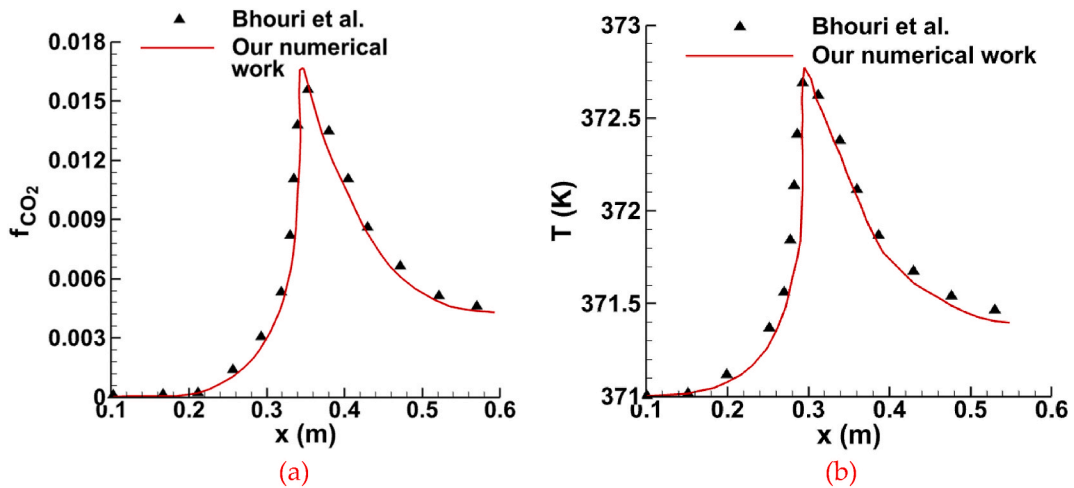
Fig. 5. Verification of numerical model; (a) CO_2 mass fraction distribution and (b) temperature profile of for $U_0 = 8$ m/s, $U_\infty = 8$ m/s.

Table 3
Studied scenarios.

Scenario	1	2	3	4	5
Wind direction	North				
u_0	35 m/s				
u_{ref}	0 m/s	3.5 m/s	5.25 m/s	7 m/s	10.5 m/s
velocity ratio R $= \frac{u_{ref}}{u_0}$	0	0,1	0,15	0,2	0,3
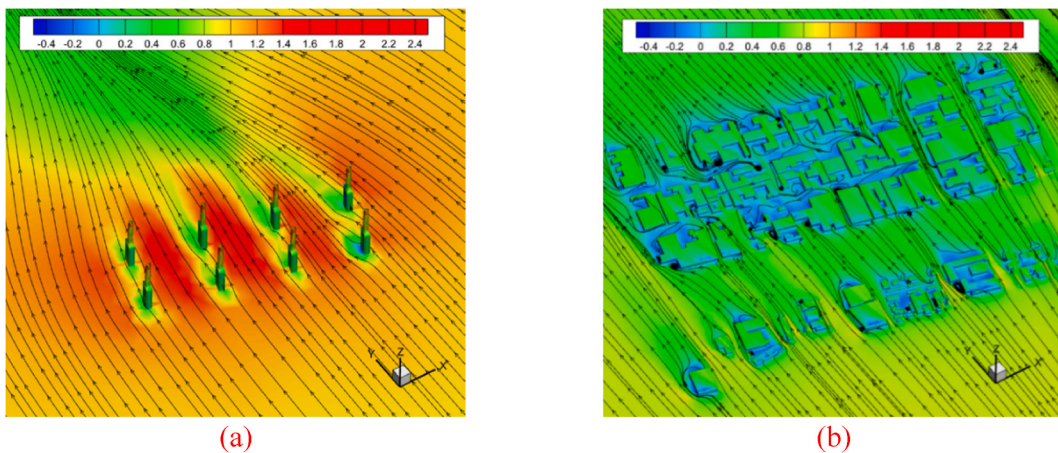
Fig. 6. Streamlines velocity contours (a) Zoom on the chimneys, (b) Zoom on the buildings at the plane Z = 1.5 m for $u_{ref} = 3.5$ m/s and $u_0 = 35$ m/s.

and measurements were performed using the particle image velocimetry (PIV) technique. Although this experimental configuration is quite simple, it can help to validate the different choices parameters of the used model. In Fig. 4 (a, b), the horizontal and vertical velocities located at 60 mm from the stack are plotted. The maximum variation between the experimental and numerical values never exceeds 8 %. This confirms the validity of our model from a hydrodynamic point of view.

Fig. 5 also shows a further comparative analysis between our numerical simulations and the work of Bhouri et al. [25,26]. The dispersion of the mass fraction of carbon dioxide (Fig. 5(a)) and the temperature profile (Fig. 5(b)) on a horizontal line just above the obstacle were plotted. Here also a very good agreement has been noted, which confirms the accuracy of our code in terms of heat and mass transfer."
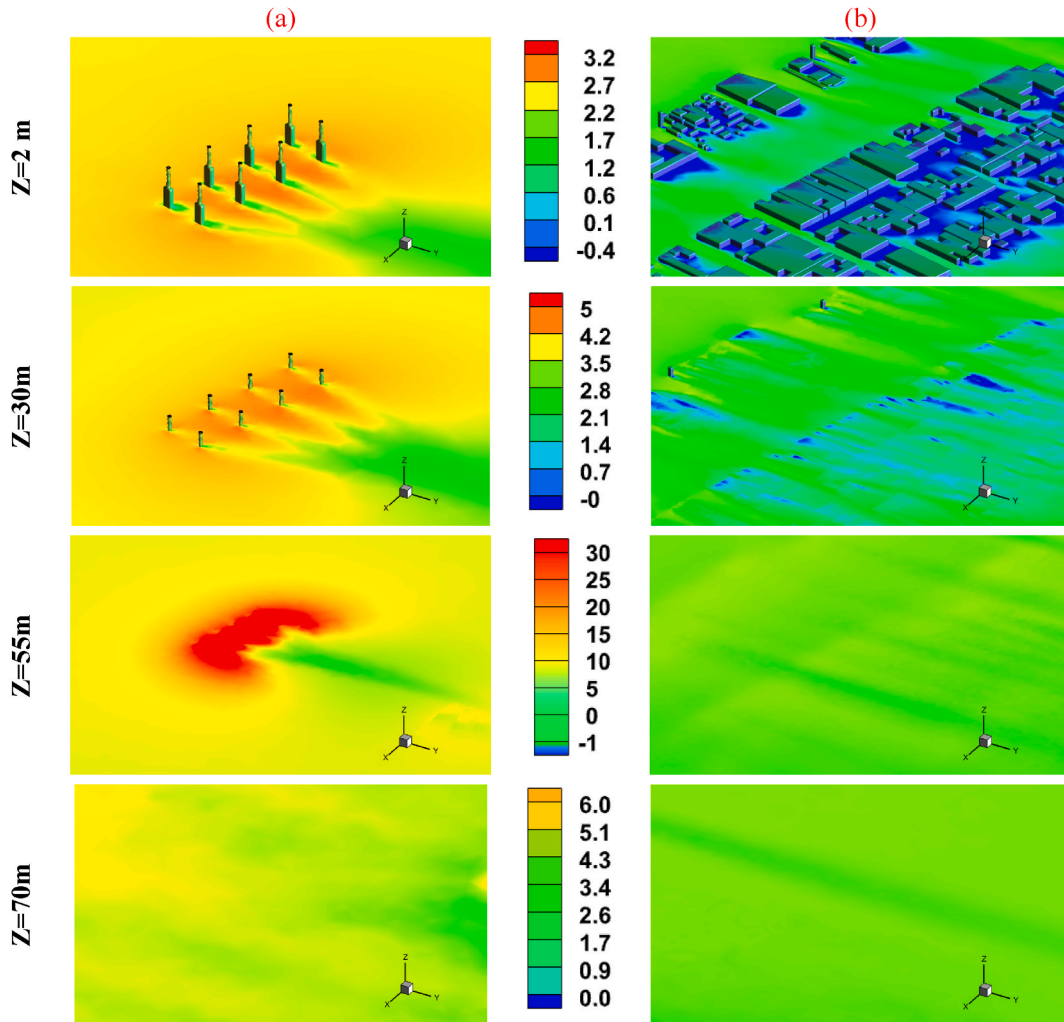
Fig. 7. Wind speed distribution according to altitude level (a) Zoom on the chimneys, (b) Zoom on the buildings for $u_{ref} = 3.5$ m/s and $u_0 = 35$ m/s.

3. Results and discussion

It is important to note that all the results are based on an effort to faithfully replicate real-world conditions. For this purpose, several parameters, such as wind direction [24] and pollutant emission velocity from the chimney, were kept constant. However, the wind velocity profile, in particular the reference velocity "u_{ref}" was varied from 0 to 10 m/s. Table 3 provides a summary of the different scenarios studied.

3.1. Flow velocity characterization

Fig. 6 (a, b) displays the streamlines' distribution, colored by the wind speed near the ground, for a velocity of $u_{ref} = 3.5$ m/s (at $z_{ref} = 10$ m). Between the chimneys, the wind speed accelerates due to the narrowing of the cross-section, whereas the opposite phenomenon occurs on the building site. Indeed, the fluid flow experiences a substantial decrease in velocity due to the highly uneven topography of the site. Additionally, several recirculation zones with reverse flow can be observed, which are caused by the wake of certain buildings.

Wind speed distribution according to altitude level is shown in Fig. 7(a and b). In the region near the chimney, where Z < 30 m, a similar behavior to that depicted in Fig. 5 is observed, characterized by an increase in air velocity between the chimneys. However, at Z = 55 m (i.e., above 15 m from the stacks) a strong intensification of flow motion is recorded due to the flue gases discharged from the chimneys. It is only when the height exceeds 70 m (Z > 70 m) that the wind flow become uniform and homogeneous. In this case, the airflow is no longer influenced by the ground or the chimneys.

On the buildings side, for Z < 35 m, the flow is slowed down, and in certain areas even stopped. This behavior is attributed to the rough topography created by the buildings. However, at altitudes exceeding 55 m, the flow becomes fully homogeneous and uniform.
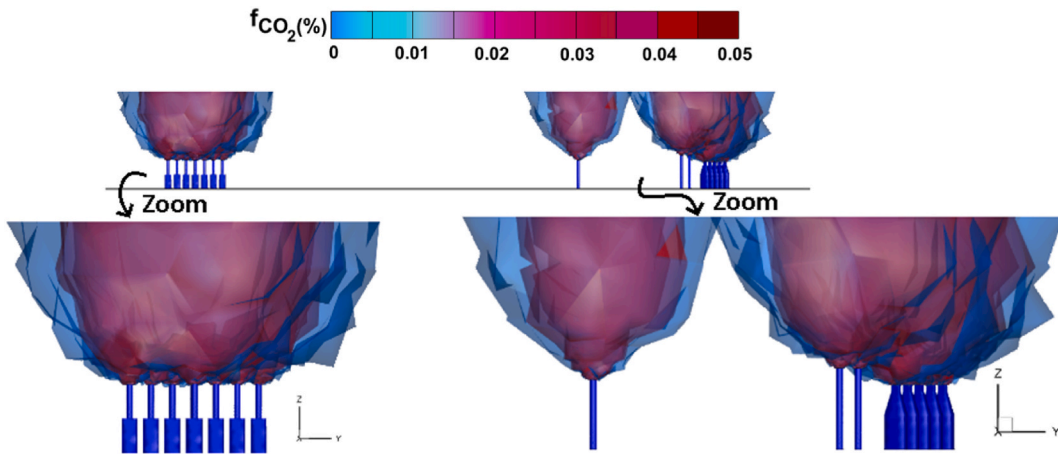
Fig. 8. Side view of CO_2 mass fraction distribution for $u_{ref} = 0$ m/s and $u_0 = 35$ m/s.
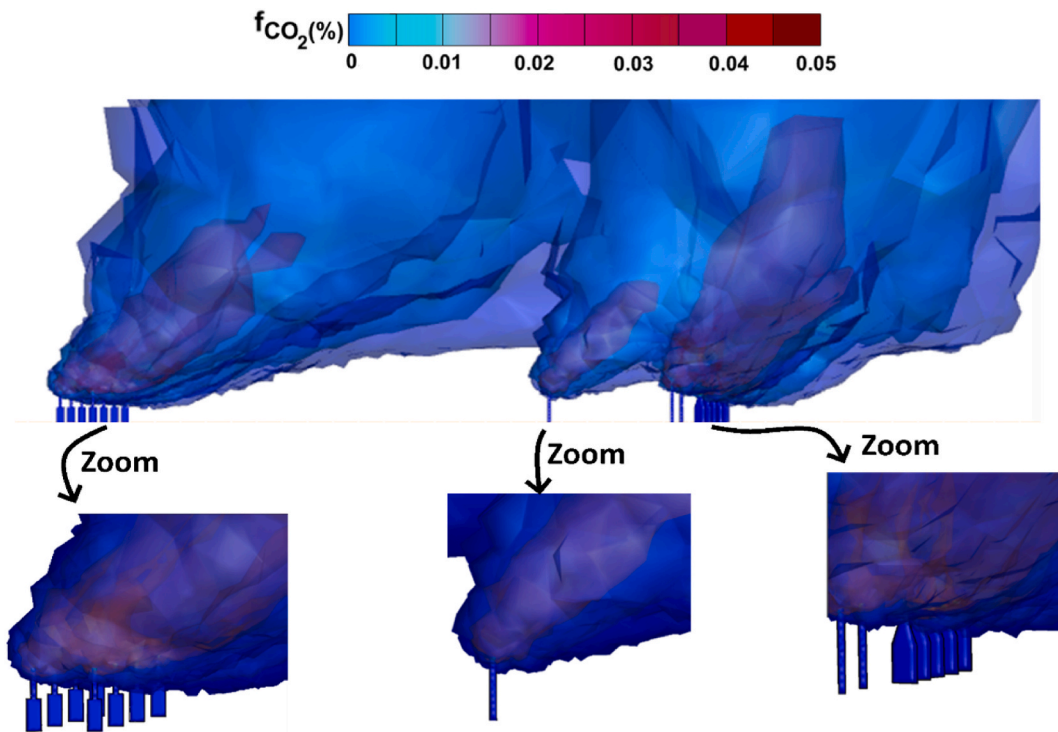

Fig. 9. Side view of CO_2 mass fraction distribution for $u_{ref} = 3.5$ m/s and $u_0 = 35$ m/s.

3.2. Pollutant characterization

As shown in Fig. 8, in the absence of wind $u_0 = 0$ (velocity ratio $R = u_{ref}/u_0 = 0$) the pollutant plumes disperse towards the upper atmospheric layers, forming a cone shape with slight horizontal diffusion. The concentration of pollutants is significantly high along the vertical lines passing through the center of the chimneys. However, no pollution risk is recorded on the ground.

For a reference wind speed of about 3.5 m/s (as shown in Fig. 9), the exhaust plume is discharged from the stack into the atmosphere with at a 45° angle (on the Z-Y plan). With such a velocity ratio $R = 0.1$, toxic gases are still unable to reach the ground and do not pose a danger to the surrounding buildings.

On the other hand, when $R = 0.2$ (Fig. 10) the velocity of the discharged pollutants loses its ability to withstand the impact and shear caused by the crosswind. As a result, it is deflected at a significant angle away from the vertical axis of the stack. Indeed, the gases released from the chimney exit are diverted directly to the north in the direction of the building. The pollutant gases follow a horizontal trajectory parallel to the ground. The plume spreads out in the shape of a wide lateral cone, exhibiting significant lateral mass
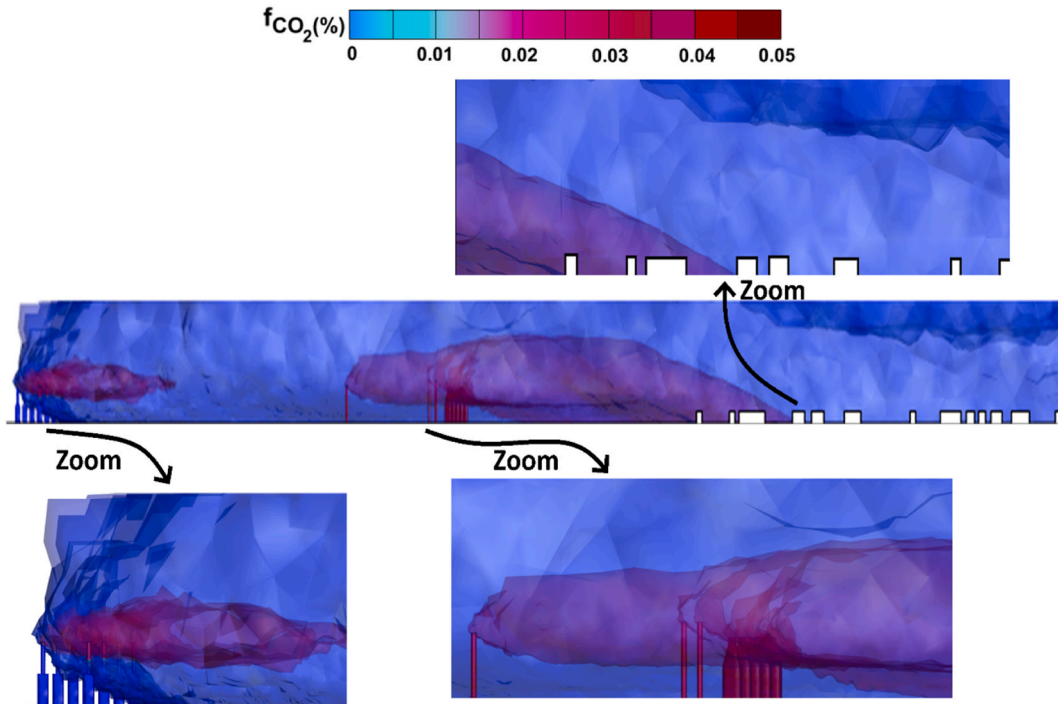
Fig. 10. Side view of CO_2 mass fraction distribution for $u_{ref} = 7$ m/s and $u_0 = 35$ m/s.
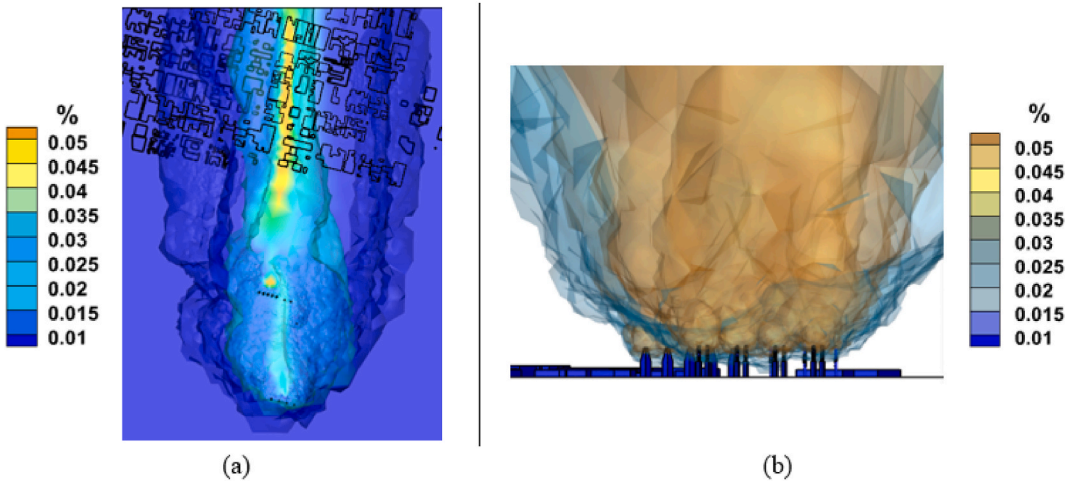

Fig. 11. CO_2 mass fraction distribution for $u_{ref} = 7$ m/s and $u_0 = 35$ m/s (a) Top view; (b) back view.

diffusion. It can also be seen that a relatively high concentration of flue gases reached the ground around the first buildings near the stack. It can be concluded that the downwash of harmful gaseous particles, induced by crosswinds, occurs when the velocity ratio 'R' exceeds a certain threshold (R > 0.18).

The different other views (lateral and top) of the CO_2 mass concentration presented in Fig. 11 (a and b) confirm the strong transverse and longitudinal mass diffusion of the pollution as well as its important penetration into the urban building area.

Fig. 12 shows the carbon dioxide mass fraction profile for three different positions at a distance of 750 m, 1450 m and 2000 m from the stacks respectively. A significant concentration of pollutants is observed at position 1, which is the closest position to the stacks. The peak in concentration occurs at an elevation of approximately 48 m, which corresponds closely to the height of the stacks. As expected, the elevated position of the stack effectively mitigated the risk of contamination on the ground in areas near the emission sources. As the distance from the stacks increases, the intensity of the peak gas concentration diminishes due to the process of dilution with air. However, it was observed that there is a higher concentration of gases on the ground, which can be attributed to mass
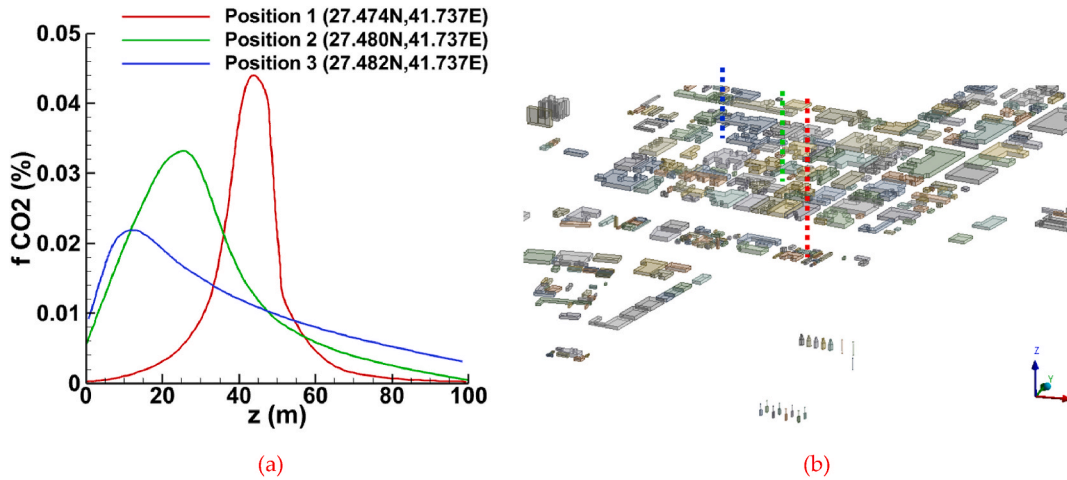
Fig. 12. (a) CO_2 mass fraction profile as a function of altitude at different position around building for $u_{ref} = 7$ m/s and $u_0 = 35$ m/s; (b) selected positions.
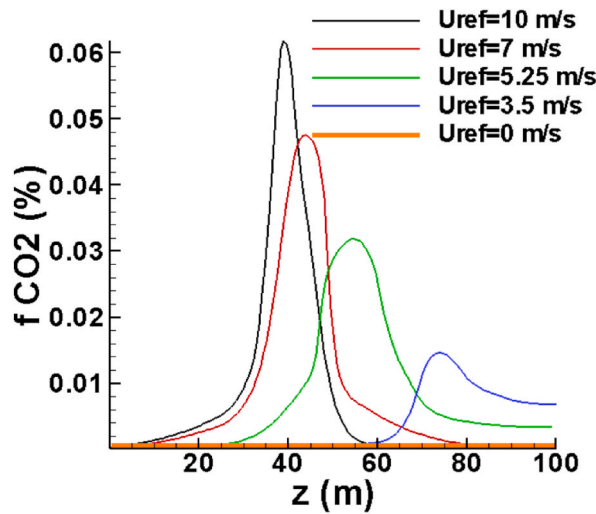

Fig. 13. CO_2 mass fraction profile as a function of u_{ref} for position 1 and $u_0 = 35$ m/s.

diffusion. In fact, as the plume cone expands, pollutant particles gradually settle on the Earth's surface.

Fig. 13 displays the profile of the carbon dioxide mass fraction at position 1 for different wind velocities. For very calm wind conditions (uref = 0), the pollution disperses into the atmosphere, and no pollution is detected in the vicinity of the buildings.

By increasing the wind velocity to 3.5 m/s, the pollution reaches position 1 with a relatively moderate fraction, approximately 0.01–0.015 %. This pollution is mainly localized at higher altitudes, starting from 70 m above the Earth's surface.

As the wind speed increases, the concentration of pollutants at the peak becomes higher and its altitude gets closer to the height of the chimney, typically around 40 m/s. Furthermore, the increase in "u_{ref}" restricts the diffusion of pollutants to higher altitudes.

4. Conclusion

This paper presents the results of a computational simulation conducted using the ANSYS FLUENT 19.2 software. The study focuses on the dispersion of pollutants generated by fuel combustion in a thermal power plant situated in the Hail region (Saudi Arabia).

Under realistic meteorological conditions, an investigation was conducted to analyze the distribution of wind speed and the concentration of pollutants, particularly the carbon dioxide mass fraction. The results indicate that at a reference wind speed of approximately 7 m/s in the northward direction, there is a significant accumulation of pollutants (with a concentration ranging from 0.01 % to 0.02 %). These pollutants can potentially infiltrate residential structures, posing potential health hazards.

It is important to note that this study has certain specificities. In addition to the arid and dry climate conditions, the computational domain size is very large, covering more than 500 ha. Although the studied area does not encompass the entire city of Hail, it still

represents a significant portion of the town's surface area.

In the continuity of this work, it would be worthwhile to explore possible solutions to mitigate the hazards of this pollution. Four potential options could be simulated:

- Carefully select and optimize chimneys dimensions, specifically the diameter (to adjust the ejection velocity) and height (to control the injection altitude).
- Optimize the arrangement of chimney positions for better pollution dispersion.
- Explore the possibility of reducing the number of emission sources from 16 to 3, it is technically feasible to consolidate neighboring chimney sets into a single larger one.
- Study the effect of adding vegetation on the dispersion of pollution.

Author contribution

Walid Hassen: Nidhal Hnaien: Lotfi Ben Said: Faris Mohammed Albati: Badreddine Ayadi: Wajdi Rajhi: Lioua Kolsi: Conceived and designed the experiments; Performed the experiments; Analyzed and interpreted the data; Contributed reagents, materials, analysis tools or data; Wrote the paper.

Data availability statement

Data included in article/supplementary material/referenced in article.

Declaration of competing interest

The authors declare that they have no known competing financial interests or personal relationships that could have appeared to influence the work reported in this paper.

Acknowledgements

References

[1] S.T. Cuffe, R.W. Gerstle, A.A. Orning, Air pollutant emissions from coal-fired power plants report no. 1, J. Air Waste Manag. Assoc. 14 (2012) 353–362, https://doi.org/10.1080/00022470.1964.10468295.
[2] J.H. Amorim, V. Rodrigues, R. Tavares, J. Valente, C. Borrego, CFD modelling of the aerodynamic effect of trees on urban air pollution dispersion, Sci. Total Environ. 461 (2013) 541–551, https://doi.org/10.1016/j.scitotenv.2013.05.031.
[3] M. Taleghani, A. Clark, W. Swan, A. Mohegh, Air pollution in a microclimate; the impact of different green barriers on the dispersion, Sci. Total Environ 711 (2020), 134649, https://doi.org/10.1016/j.scitotenv.2019.134649.
[4] A. Tiwari, P. Kumar, R. Baldauf, K.M. Zhang, F. Pilla, S.D. Sabatino, E. Brattich, B. Pulvirenti, Considerations for evaluating green infrastructure impacts in microscale and macroscale air pollution dispersion models, Sci. Total Environ. 672 (2019) 410–426, https://doi.org/10.1016/j.scitotenv.2019.03.350.
[5] Y. Xing, P. Brimblecombe, Role of vegetation in deposition and dispersion of air pollution in urban parks, Atmos. Environ. 201 (2019) 73–83, https://doi.org/10.1016/j.atmosenv.2018.12.027.
[6] G. Sharmilaa, T. Ilango, A review on influence of age of vehicle and vehicle traffic on air pollution dispersion, Mater, Today Off.: SAVE Proc. 60 (2022) 1629–1632, https://doi.org/10.1016/j.matpr.2021.12.188.
[7] V.T. Olga, V.M. Sergey, A. Pitt, A.L. Anatoly, V.Z. Yuri, Air pollution dispersion within urban street canyons, Atmos. Environ. 43 (2009) 245–252, https://doi.org/10.1016/j.atmosenv.2008.09.076.
[8] Y. Shi, X. Xie, J.C.H. Fung, E. Ng, Identifying critical building morphological design factors of street-level air pollution dispersion in high-density built environment using mobile monitoring, Built. Environ. 128 (2018) 248–259, https://doi.org/10.1016/j.buildenv.2017.11.043.
[9] E. Aristodemou, L.M. Boganegra, L. Mottet, D. Pavlidis, A. Constantinou, C. Pain, A. Robins, H. ApSimon, How tall buildings affect turbulent airflows and dispersion of pollution within a neighborhood, Environ. Pollut. 233 (2018) 782–796, https://doi.org/10.1016/j.envpol.2017.10.041.
[10] H. Wen, L. Malki-Epshtein, A parametric study of the effect of roof height and morphology on air pollution dispersion in street canyons, J. Wind Eng. Ind. 175 (2018) 328–341, https://doi.org/10.1016/j.jweia.2018.02.006.
[11] T. Banerjee, S.C. Barman, R.K. Srivastava, Application of air pollution dispersion modeling for source-contribution assessment and model performance evaluation at integrated industrial estate-Pantnagar, Environ. Pollut. 159 (2011) 865–875, https://doi.org/10.1016/j.envpol.2010.12.026.
[12] A. Issakhov, A. Alimbek, A. Issakhov, A numerical study for the assessment of air pollutant dispersion with chemical reactions from a thermal power plant, Eng. Appl. Comput. Fluid Mech. 14 (2020) 1035–1061, https://doi.org/10.1080/19942060.2020.1800515.
[13] H. Gourgue, A. Aharoune, A. Ihlal, Study of the air pollutants dispersion from several point sources using an improved Gaussian model, J. Mater. Environ. Sci. 6 (2015) 1584–1591.
[14] N.M. Lopes Romeiro, E.R. Cirilo, P.L. Natti, L.M.D. Okamoto, T. Julianotti, Chimney height, a determining factor in the dispersion of pollutants and their concentration, World J. Eng. 9 (2020) 173–193, https://doi.org/10.4236/wjet.2021.91013.
[15] A.O. Dawood, A.J. Sangoor, A.H.J. Al-Rkaby, Behavior of tall masonry chimneys under wind loadings using CFD technique, Case Stud. Constr. Mater. 13 (2020), e00451, https://doi.org/10.1016/j.cscm.2020.e00451.
[16] H. Gourgue, A. Aharoune, A. Ihlal, Dispersion of the nox emissions from chimneys around industrial area: case study of the company cibel II, Mater. Today: Proc. 2 (2015) 4689–4693, https://doi.org/10.1016/j.matpr.2015.09.024.
[17] F. Zair, M. Mouqallid, E.H. Chatri, Factors impact the dispersion of pollutants emitted from the bent chimney around the obstacles, AIP Conf. Proc. 2345 (2021), 020014, https://doi.org/10.1063/5.0049495.
[18] F. Zair, M. Mouqallid, E.H. Chatri, The effect of straight chimney temperature on pollutant dispersion, E3S Web Conf. 234 (2021), 00009, https://doi.org/10.1051/e3sconf/202123400009.

[19] N.M. Said, H. Mhiri, G. LePalec, P. Bournot, Experimental and numerical analysis of pollutant dispersion from a chimney, Atmos. Environ. 39 (2005) 1727–1738, https://doi.org/10.1016/j.atmosenv.2004.11.040.

[20] Y. Liu, T. Ming, C. Peng, Y. Wu, W. Li, R.D. Richter, N. Zhou, Mitigating air pollution strategies based on solar chimneys, Sol. Energy 218 (2021) 11–27, https://doi.org/10.1016/j.solener.2021.02.021.

[21] M.M. Esmaili, S.H. Fallah, M. Izanlu, M.S. Valipour, Investigation on the Performance of a solar chimney-flare gas hybrid system, Sustain. Energy Technol. Assessments 52 (2022), 102279, https://doi.org/10.1016/j.seta.2022.102279.

[22] T. Gong, T. Ming, X. Huang, R.K. de Richter, Y. Wu, W. Liu, Numerical analysis on a solar chimney with an inverted U-type cooling tower to mitigate urban air pollution, Sol. Energy 147 (2017) 68–82, https://doi.org/10.1016/j.solener.2017.03.030.

[23] M.L. Ray, A.L. Rogers, J.G. McGowan, Analysis of Wind Shear Models and Trends in Different Terrain, University of Massachusetts, Department of Mechanical and Industrial Engineering, Renewable Energy Research Laboratory, 2006.

[24] N. Hnaien, W. Hassen, L. Kolsi, A. Mesloub, M.A. Alghaseb, K. Elkhayat, M.H.H. Abdelhafez, CFD analysis of wind distribution around buildings in low-density urban community, Mathematics 10 (2022) 1118, https://doi.org/10.3390/math10071118.

[25] I.B. Baouab, N. Mahjoub Said, H. Mhiri, G. LePalec, P. Bournot, Experimental and numeric study of flow around a parallelepiped obstacle issued from a bent chimney, Defect Diffus. Forum Trans 283 (2009) 346–351, https://doi.org/10.4028/www.scientific.net/DDF.283-286.346.

[26] I.B. Baouab, N. Mahjoub Saïd, H. Mhiri, P. Bournot, G. LePalec, Dynamic and mass transfer characteristics of the flow issued from a bent chimney around buildings, Heat Mass Tran. 49 (2013) 337–358, https://doi.org/10.1007/s00231-012-1078-7.